RSC Advances

RSC Publishing

PAPER

View Article Online
View Journal

Cite this: DOI: 10.1039/c3ra44301a

Highly photoactive heterostructures of PbO quantum dots on TiO_2†

A. Leelavathi,[a] B. Mukherjee,[b] C. Nethravathi,[b] Subhajit Kundu,[b] M. Dhivya,[b] N. Ravishankar*[b] and Giridhar Madras[a]

Received 11th August 2013
Accepted 30th August 2013

DOI: 10.1039/c3ra44301a

www.rsc.org/advances

We present a non-hydrolytic sol–gel combustion method for synthesizing nanocomposites of PbO quantum dots on anatase TiO_2 with a high surface area. XRD, electron microscopy, DRS, cathodoluminescence and BET were employed for structural, microstructural and optical characterization of the composites. The photocatalytic activity of TiO_2 and PbO/TiO_2 was investigated and compared with Degussa P-25. The results indicate that the photocatalytic activity of quantum dot dispersed TiO_2 is higher than that of bare TiO_2 and much higher than that of commercial Degussa P-25. The origin of enhanced photoreactivity of the synthesized material can be assigned to a synergetic effect of high surface area, higher number of active sites and an engineered band structure in the heterostructure. The mechanisms for photocatalytic activity are discussed based on production of photogenerated reactive species. The knowledge gained through this report open up ideal synthesis routes for designing advanced functional heterostructures with engineered band structure and has important implications in solar energy based applications.

Introduction

The development of highly photoactive materials is important to solve the energy crisis and reduce environmental pollution. Since the report by Honda and Fujishima,[1] TiO_2 based material have been extensively utilized with regard to photodegradation of environmental pollutants.[2,3] TiO_2 is highly photoactive, has a strong oxidizing potential, long term photostability and is also economical.[4] Several research efforts have been directed towards modifying TiO_2 to exhibit visible light photocatalytic activity.[5–8] The photocatalytic activity of TiO_2 depends on many parameters such as size,[2] porous structure with high surface area[9,10] and the presence of photoactive exposed facets.[11–13] Many reports have revealed that particles with higher density of hydroxyl group,[14–16] appropriate crystal phase(s), defect level,[17] band gap and energy level alignment in the case of heterostructures could significantly enhance the activity.[18] However, the efficiency of this material is limited due to lack of isolation of photogenerated charge carriers. One practical approach to reduce the recombination probability of e^-/h^+ pairs is by making a composite of TiO_2 with other semiconductor materials. Engineering composites oxide nanomaterials with suitable band alignment is expected to favor the separation of generated charge carriers.[19,20] Composite heterostructures with favorable band alignment have variety of applications such as catalysts, sensors, solar and photoelectrochemical cells.[21–23]

TiO_2 is known to have three major polymorphs, anatase (tetragonal), brookite (orthorhombic) and rutile (tetragonal).[24] Among TiO_2 polymorphs, anatase has higher photocatalytic activity.[25] Based on experimental and theoretical observations, anatase phase has been proven to be desirable phase than rutile at very small crystal size. Investigations have shown that mixed phase TiO_2[26] with appropriate weight ratio showed better performance than desired anatase phase alone. The synergistic effect in mixed phase arises presumably from efficient charge transfer and separation achieved through staircase like band alignment (type II) despite the fact that both phases have similar band gap energy. Therefore in spite of the similarity with sensitized system from type II band alignment, the enhancement mechanism actually arises from charge separation and utilization in the UV region and not necessarily extended to the visible spectrum. This is due to favorable separation of photogenerated charge carriers, as in the case of P-25 Degussa.[27] Zhu *et al.* investigated the photocatalytic activity of heterostructured TiO_2 (B)/TiO_2 anatase.[28] They showed that the composite phases of TiO_2 with suitable band edge positions showed higher activity than single phase of TiO_2.[28] Composites with suitable band energy level of designed heterostructures has attracted considerable attention towards photocatalysis.[21,22]

[a]*Centre for Nanoscience and Engineering, Indian Institute of Science, Bangalore, 560012, India*

[b]*Materials Research Centre, Indian Institute of Science, Bangalore, 560012, India. E-mail: nravi@mrc.iisc.ernet.in; Fax: +91 80 23607316; Tel: +91 80 22933255*

† Electronic supplementary information (ESI) available: Fig. S1: HRTEM micrograph of PbO/TiO_2 shows that *d*-spacing of 2.8 Å corresponding to the (200) plane of PbO. Fig. S2: EDS spectra of PbO/TiO_2 composite showing presence of Pb, Ti, O and with almost 10 mol% of PbO. Fig. S3: XPS Ti 2p spectra of synthesized materials. See DOI: 10.1039/c3ra44301a

Inspired by these results, it is meaningful to engineer heterostructures of TiO_2 anatase coupled with other semiconductors. A similar concept has been applied to propose a biphasic multimetal oxide composite with the objective to create (i) thermally and chemically more stable composite than chalcogenide based composites (ii) charge separation induced generation of more reactive holes (having higher energy) for oxidative degradation of dyes (iii) better enhancement in the UV region compared to multiphasic TiO_2 composites. This can be further subjected to co-sensitization with other sensitizers to extend its visible light activity. So far, reports available on coupled semiconductors are type II band alignment mainly focused as sensitized system for narrowing band gap. Our report describes an efficient separation of photogenerated charge carriers in TiO_2 with the help of heterostructure like P-25 Degussa.

Based on the above studies, we have designed composites of PbO quantum dot dispersed on faceted nanoparticles of anatase TiO_2 with a favorable band edge alignment for the separation of generated charge carriers. We report a facile method that combines non-hydrolytic sol–gel and combustion methods to prepare quantum dot dispersed on TiO_2, to form heterostructures. Non-hydrolytic sol–gel with slow reaction kinetics[29] leads to the formation of nanoparticles of faceted TiO_2. Therefore, combining both non-hydrolytic sol–gel and combustion techniques leads to formation of uniform dispersion of PbO quantum dot on faceted nano anatase with high surface area. A non-hydrolytic sol–gel combustion technique of a biphasic mixture has been adopted in the current work to (i) ensure physically separated polycondensation of metal complexes followed by combustion leading to an intimate mixture of different metal oxide in the structure (ii) high temperature during combustion leads to better crystallization with restricted crystal growth achieved through better and uniform separation in metal-complex biphasic mixture. Combustion synthesis eliminates organics and yields well developed porous morphology with high surface area.[30] Further, our method for composite heterostructures provides very good interface between two exposed crystals. Such interface could render high photoactivity with efficient photogenerated charge transfer between them. Using this method, high surface area composites of PbO/TiO_2 was prepared. These composites make type II band alignment resulting in a highly photoactive material and the mechanism for this photocatalytic activity is explained.

Experimental

Synthesis of TiO_2

The synthesis of TiO_2 was accomplished using a single step sol–gel combustion method. Titanium tetraisopropoxide (TTIP) was mixed with oleic acid and oleylamine in the ratio of (1 : 2 : 1),[30] followed by addition of 100 μL water. The obtained mixture was transferred to 60 mL Teflon vessel. This was sealed in a stainless steel autoclave, and then heated at 280 °C for 3 h for partial poly-condensation of the precursors. The resultant solution was subjected to combustion at 350 °C for 5 min to obtain a porous structure. The obtained black powder was ground well using mortar and pestle, followed by annealing for 2 h at 400 °C. Finally, the obtained white powders were washed with ethanol, and then dried at room temperature.

Synthesis of PbO/TiO_2 nanohybrids

(i) Preparation of Pb myristate salt. Pb myristate salt was prepared by mixing lead acetate with myristic acid in 1 : 2 molar ratio. This mixture was heated at 150 °C for 1 h to obtain an optically clear homogeneous solution. The solution was then cooled to room temperature to obtain a grey waxy solid, followed by recrystallization in toluene.

(ii) Preparation of PbO/TiO_2 composite. This involves two steps, as follows:

Titanium tetraisopropoxide TTIP (13.5 mL, 50 mM) was mixed with oleic acid (30 mL) in the ratio of 1 : 2. Water (100 μL) was added to the above mixture; the obtained mixture was transferred to Teflon vessel. This was sealed in a stainless steel autoclave, and then heated at 280 °C for 30 min to obtain partial poly-condensation of TTIP complex (solution A).

The above prepared lead myristate salt (5 mmol) was dissolved in oleylamine (15 mL), and then heated at 80 °C for 2 min to get clear solution. Water (200 μL) was added to the above clear solution (solution B).

Solution B was added to solution A that contains the partially condensed Ti precursor. This reaction mixture was transferred to Teflon vessel and sealed in a stainless steel autoclave, then subjected to 280 °C for 3 h. The solvent rich phase was discarded after centrifugation. The pale yellow gelatinous phase obtained was subjected to combustion at 350 °C for 5 minutes to get porous composite oxides. The obtained powder was ground well using mortar and pestle, followed by annealing for 2 h at 400 °C. Finally, the pale yellow powder obtained was washed with ethanol, and then dried at room temperature.

Characterization

Transmission electron microscopy (TEM) images were acquired with a Tecnai T20 operated at 200 kV. The samples were prepared by drop casting a sample dispersed in ethanol on carbon coated Cu-grids and dried in a vacuum. Powder X-ray diffraction (XRD) was carried out using Phillips X'pert diffractometer with Cu Kα radiation. Room temperature cathodoluminescence (CL) spectra were measured using a Gatan Mono CL 3 system installed on a Zeiss Ultra55 FESEM. The surface area and pore size distribution was determined by Brunauer–Emmett–Teller (BET) method using Quantachrome NOVA 1000 analyzer by nitrogen adsorption–desorption method at liquid nitrogen temperature. X-ray photoelectron spectra (XPS) of the samples were collected on an Axis Ultra using monochromatic source of Al Kα radiation. The diffuse reflectance spectra were obtained using solid state UV spectroscopy (Perkin Elmer) with integrated sphere. The photoluminescence spectrophotometer (LabRAM HR) was used to measure the emission intensity of 2-hydroxyterephthalic acid formed with the help of CCD detector.

Photoreactor

The photocatalytic experiments were carried out in a slurry reactor. The photoreactor consists of two parts, quartz jacketed tube where lamp was placed inside the tube and Pyrex reactor in which dye solution and catalyst suspension were taken. The catalysts (1 g L^{-1}) were dispersed in 50 ppm of orange G aqueous dye solution and continuously stirred to ensure uniform dispersion of catalyst during reaction. Water was circulated through the annulus of both Pyrex reactor and quartz tube to maintain the dye solution at 30 °C. A metal halide lamp of 400 W in the spectral range 300–700 nm with incident intensity of 1.79 μ Einstein per L per s and photon flux of 8.86 W m^{-2} was used. This spectrum is similar to the solar spectra. Experiments were also conducted with an UV lamp (wavelength maxima at 365 nm).

The dye degradation was determined by analyzing dye solution at periodic intervals using UV-vis spectrophotometer (Shimadzu, 1700 UV-VIS).

Photocurrent measurements

Solar simulator class 3A (Oriel Sol 3A) equipped with a xenon lamp with 1.5 air mass (AM) and operated at 450 W was used. The samples were made into a cylindrical pellet and silver paste, copper wire was used as a contact for measurement. Two probe photocurrent measurements were carried out with the help of Keithley source meter (Model no. 2420).

Results and discussion

A schematic illustration of synthesis of PbO dispersed on TiO_2 is shown in Fig. 1. The first step *viz.*, the sol–gel condensation of Ti–oleate complex, followed by thermolytic decomposition of Pb myristate with oleylamine complex leads to formation of PbO on Ti–O network. The second step involves the removal of organic residues through combustion method that resulted in nanocomposites of PbO dispersed on TiO_2 structure. This step also leads to porous morphology with high surface area.[31–33] Sol–gel condensation and thermolytic decomposition of an organic biphasic mixture of Ti–oleate complex and Pb-myristate and oleylamine complex where they reside in different phases results in uniform PbO dispersed on TiO_2.

As reported, highly viscous partially condensed yellow Ti–oleate complex was formed by adding TTIP with oleic acid.[34] The heating process (260 °C) leads to replacement of one or more isopropoxide with oleate ligand and release of isopropyl alcohol. In the second step, heating with addition of oleylamine leads to aminolysis reaction. This leads to the formation of unstable hydroxyalkoxides through nucleophilic attack of oleylamine on Ti–oleate complex.[34] Finally, this resulted in polymeric Ti–O–Ti network bound by carboxylates. The addition of Pb myristate to oleylamine form octahedral complex in the case of composite synthesis.[35,30] Under solvothermal condition, thermolysis of Pb-precursor leads to the formation of PbO quantum dot on Ti–O–Ti network.

The unique feature of this biphasic mixture, when compared to other methods, is that two metal ions (Ti, Pb) stays in different phase and thereby results in a reduced possibility of intermixing of metal ions.

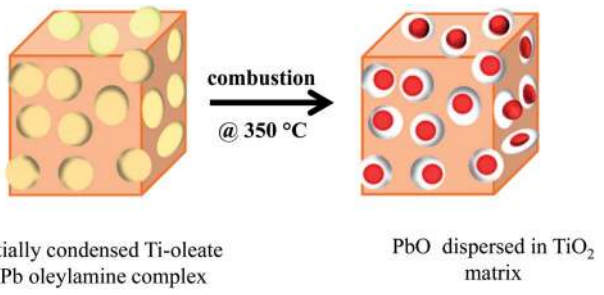

Fig. 1 Schematic illustration of synthesis strategy for uniform dispersion of PbO quantum dot on TiO_2 phase *via* sol–gel combustion method.

Structure and microstructure

Fig. 2 shows the powder XRD patterns of as-synthesized anatase and PbO/TiO_2. The diffraction peaks correspond to the anatase phase of TiO_2 (JCPDS #21-1272). In the case of composite oxides, the presence of extra asymmetric peak at 2θ values of 28.5 and 31.7 matches with PbO (JCPDS # 78-1666) and confirms the formation of orthorhombic PbO.

Transmission electron microscope (TEM) images of TiO_2 and the nanohybrids are shown in Fig. 3. Fig. 3a and b indicate that faceted TiO_2 nanocrystals ranging of 8–14 nm are obtained.[30] It has been suggested earlier that non-hydrolytic synthesis is a slow process that usually leads to the formation of faceted particles.[29] The spherical shape of anatase TiO_2 has a higher energy than faceted particles.[36] In our case, oleylamine and oleic acid bind to the {101} and {001} planes, respectively[37,38] resulting in truncated rhombohedra tiny particles[39] (as shown in Fig. 3b). HRTEM image (Fig. 3b) shows a *d*-spacing of 0.35 nm, which corresponds to (101) plane of TiO_2. Fig. 3c and d shows the bright field TEM image of PbO/TiO_2 nanohybrid in which particles exhibiting

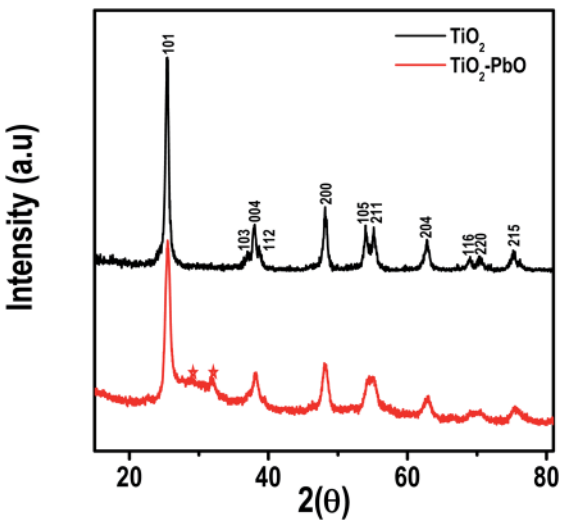

Fig. 2 Powder XRD pattern of synthesized TiO_2 confirms pure anatase phase and showing the presence of orthorhombic PbO in the composite heterostructure.

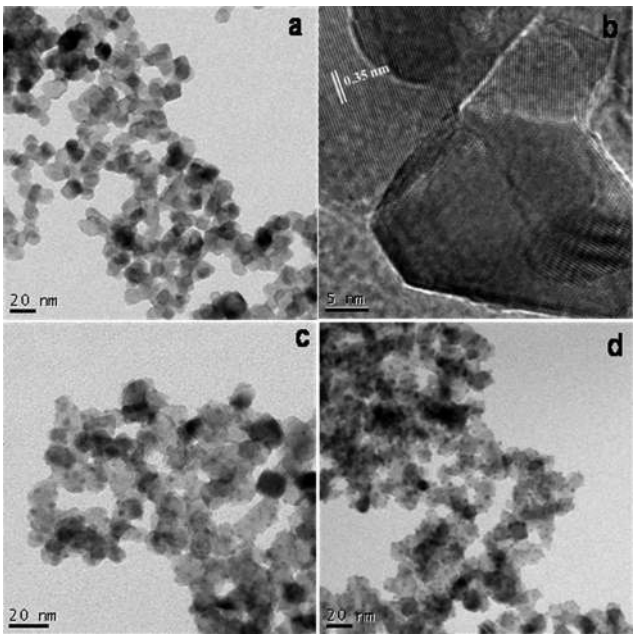

Fig. 3 (a) TEM micrograph of as-synthesized TiO_2, (b) HRTEM reveals showing fringes corresponding to the (101) plane of TiO_2, (c) and (d) bright field image of quantum dot dispersed TiO_2.

darker contrast (~6 nm or less) appear uniformly coated on the TiO_2. HRTEM image of the synthesized composites with lattice spacing of 0.28 nm corresponding to the (200) plane of orthorhombic PbO are shown in Fig. S1 (ESI†). Both the oxides are highly crystalline, as evident from HRTEM images from several regions. SEM-EDS (Fig. S2†) shows that 10 mol% loading of PbO on TiO_2, which matches with the initial precursor concentrations and indicates that the PbO is uniformly distributed on TiO_2.

Optical properties

Fig. 4 shows the UV-visible diffuse reflectance spectra of the synthesized materials as compared with P-25 Degussa. All the materials exhibited absorption edges around 400 nm corresponding to a band gap value of 3.1 eV. In the case of composite, the increase in the absorption above 400 nm can be attributed to the presence of PbO. The band gap absorption edge in the visible range is determined to be 2.6 eV, which is consistent with the orthorhombic PbO phase, as shown in the inset of Fig. 4.[40] The band gaps were also determined based on the Tauc plot and the values were the same as that determined from the absorption edges.

XPS was employed to determine the oxidation states of various species present in the synthesized materials. The XPS spectra of Ti 2p, Pb 4f and O 1s for the synthesized sample are shown in Fig. S3† and 5. As can be seen from the Fig. S3 (see ESI†), similar peak positions in Ti 2p spectra, which are taken without and with PbO loading on TiO_2. The peaks at 458.8 eV and 464.5 eV correspond to Ti $2p_{3/2}$ and Ti $2p_{1/2}$, respectively which are characteristic of Ti^{4+} states.[41] The high resolution O 1s spectra for synthesized samples are shown in Fig. 5a, which can be deconvoluted into three peaks. The peaks with binding energies of 530.1 eV, 531.5 eV and 532.7 eV can be assigned to O^{2-}, OH^- and C–O in TiO_2, respectively.[42] In the case of composite (Pb 4f spectra shown in the Fig. 5b) peaks at 138.8 eV and 143.8 eV correspond to Pb(II) oxidation states of Pb $4f_{7/2}$ and Pb $4f_{5/2}$, respectively.[43]

Porous morphology

Fig. 6 shows the N_2 adsorption and desorption isotherm for as-synthesized materials and its pore size distribution calculated from desorption curve by BJH method.

The calculated surface areas are 57 and 71 $m^2\ g^{-1}$ for TiO_2 and TiO_2–PbO nanohybrid, respectively. The increased surface area in the case of composite might be due to smaller size of dispersed PbO. The hysteresis between adsorption and desorption curves, shown in the Fig. 6a, demonstrates H1 type isotherm, which is indicative of narrow distribution of uniform pores (IUPAC classification).[44] In the case of composite oxides, bimodal pore size distribution indicates the presence of two types of mesopores, as shown in Fig. 6b (red curve). The voids size ranges from 2–12 nm and 12–35 nm for TiO_2 and PbO, respectively.

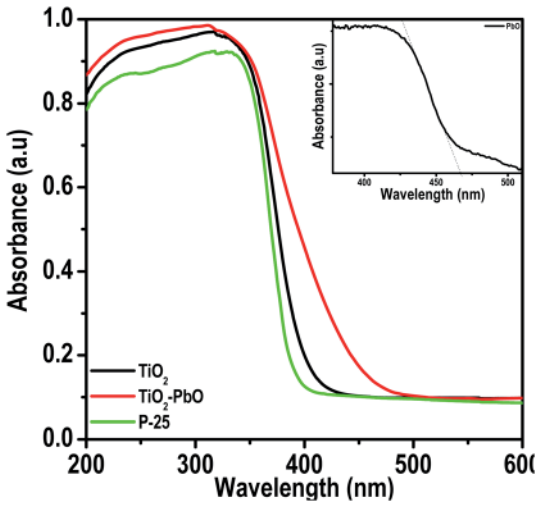

Fig. 4 Diffuse reflectance UV-visible spectra for synthesized materials and P-25 Degussa. Inset shows the DRS of synthesized PbO.

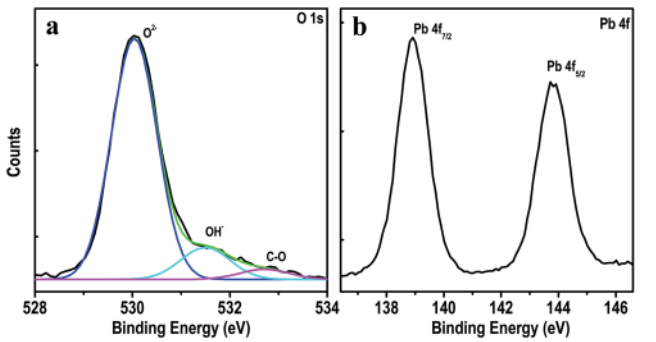

Fig. 5 XPS spectra of (a) O 1s of TiO_2 indicating the presence of different types of oxygen species and (b) Pb 4f of the composite.

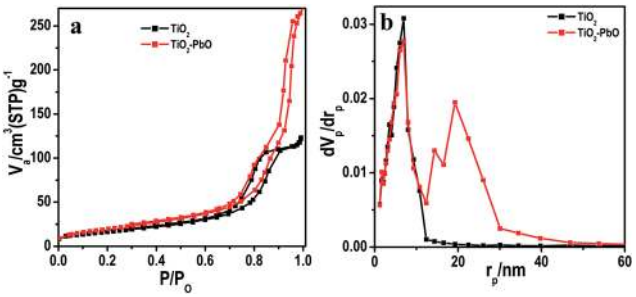

Fig. 6 (a) N_2 adsorption and desorption BET isotherm for synthesized samples and its pore size distribution (b) indicating bimodal pore size distribution.

Photocatalytic activity

The photoreactivities of the synthesized materials were evaluated using degradation of orange G. As shown in Fig. 7a, rate of degradation enhanced in the presence of synthesized materials as compared to P-25 under metal halide lamp.

In the case of the nanohybrid, the activity was higher than bare TiO_2. The same photodegradation trend is also observed in the presence of UV radiation (Fig. 7b). The repeated cycles, as shown in Fig. 7c, indicate an excellent stability of the composite photocatalyst under metal halide lamp. The as-synthesized PbO showed very poor photocatalytic activity, as shown in Fig. 7a. The degradation percentages of orange G at the end of 2 h of metal halide irradiation are 77, 50 and 41 for TiO_2/PbO, TiO_2 and P-25, respectively. The mineralization percentage was also measured for the 2 h irradiated dye solution (using TOC, Shimadzu analyzer). The percentage reductions in carbon content are 8, 5 and 2 for TiO_2/PbO, TiO_2 and P-25, respectively. The enhanced performance of the composite is possibly due to the engineered band structure with less recombination of generated charge carriers, as explained in detail below.

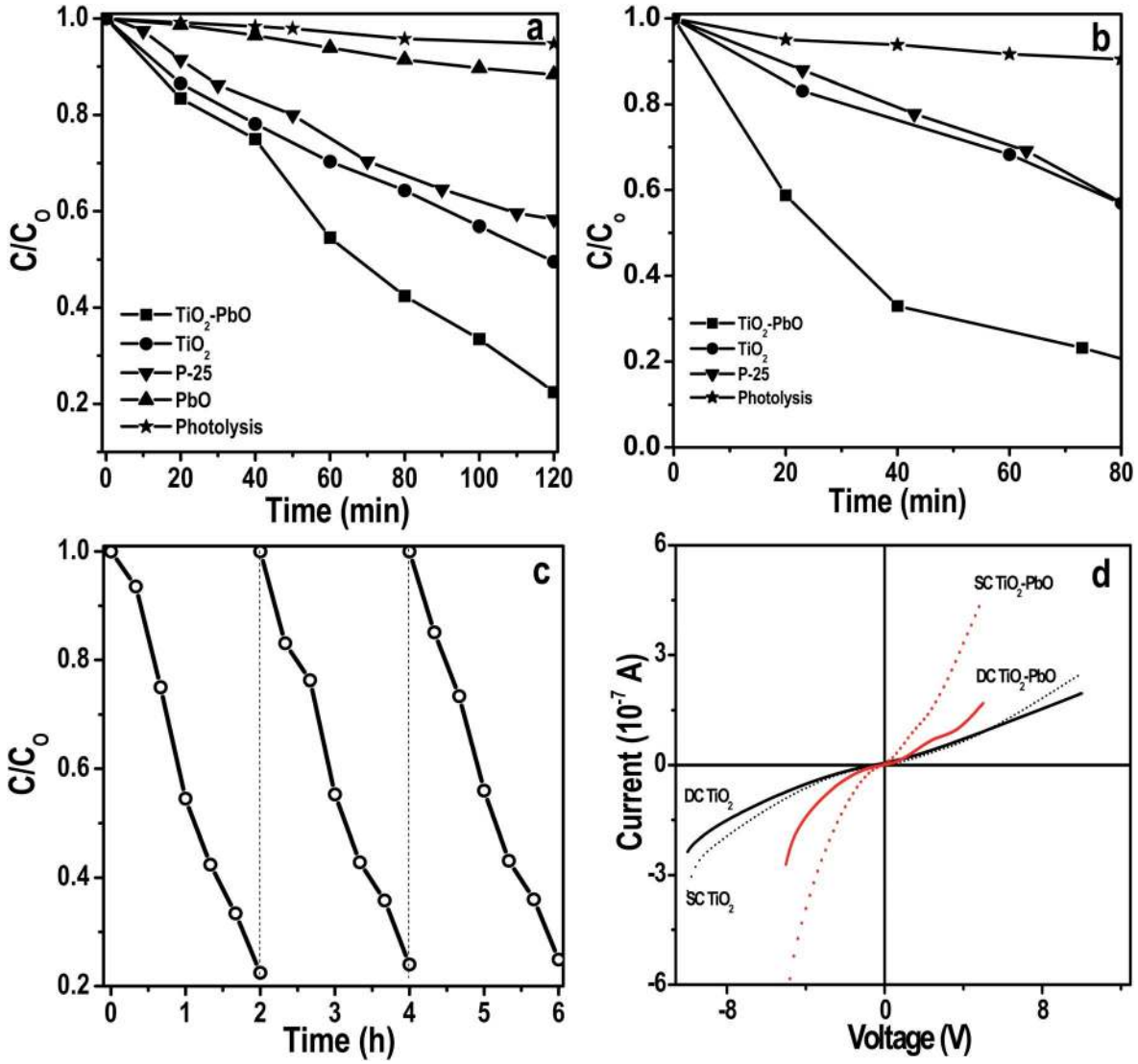

Fig. 7 Photocatalytic degradation of orange G observed as the normalized concentration *versus* time for different materials in the presence of metal halide (a) and UV lamp (b), repeated cycles of TiO_2/PbO composites indicating the stability of material towards photocatalytic activity under metal halide lamp (c) and photocurrent for the synthesized samples under solar light (d) (dark current dc, without light and solar current sc, with light).

Photocurrent measurements were studied to understand the photogenerated charge carriers under solar light. The samples were made into a pellet and then silver paste was used as contact. An enhanced photoresponse was observed for the synthesized materials. The photocurrent was higher in the case of composite, which indicate easy separation of generated charge carriers, as shown in Fig. 7d.

Origin of enhanced photocatalytic activity

The enhancement in photoreactivity might be due to synergetic effect of surface area of the synthesized structures[45] and heterostructure band energy alignment in composites. The photocatalytic process involves the following steps; generation, separation and redox reactions of generated charge carriers. The rate limiting step in photocatalysis is due to isolation of formed e^-/h^+ pairs.[3] Intimate heterostructure formed between quantum dot and TiO_2, and energy band alignment[46] makes the composites superior as compared to TiO_2 for the separation of photogenerated charge carriers. This kind of band matching facilitates the charge transfer between oxides, which induces significant activity.

Based on Mulliken electronegativity, $E_{VB} = X - E^c + 0.5E_g$, where X is the absolute electronegativity of the semiconductor, E^c is the free electron energy on hydrogen scale and E_g is the band gap of the semiconductor.[47] The calculated X values for TiO_2 and PbO are 5.81 and 5.41 eV respectively. According to the above equation, the schematic (Fig. 8) is proposed to explain the possible photogenerated charge transfer mechanisms. The drawn conduction edge potential values of TiO_2 and PbO are matching with reported values.[48] In the presence of metal halide lamp, both TiO_2 and PbO can be excited, the electrons from PbO will transfer to conduction band of TiO_2 and holes will migrate towards PbO. According to molecular orbital package (MOPAC) using the parameters of AM1/PM3 (Austin model 1/parameterized method 3) with conductor-like screening model (COMSO) calculations, the E_{LUMO} of orange G is −1.180,[49] the E_{HOMO} will lie above the valence band of PbO. Therefore, the collected holes are removed by the dye molecules from PbO, followed by direct oxidation of holes with dye because valence band edge potential of PbO is not favorable for hydroxyl radical formation (as shown in Fig. 8).

The valence band edge position of PbO is above TiO_2 so that photogenerated holes tend to migrate towards PbO from TiO_2. The calculated conduction edge position values, based on Mulliken electronegativity, matches well with the reported values.[48] It has been shown that the conduction band edge energy position of PbO is more negative than that of TiO_2 (*E vs.* NHE).[48] Therefore, this heterostructure favors charge migration and leads to separation of photogenerated charge carriers. The mechanism for enhanced photocatalytic activity in the case of composite heterostructure has been further evaluated by estimating the photogenerated intermediate radical species.

The production of photogenerated reactive hydroxyl radicals for TiO_2 and TiO_2/PbO composites was investigated by using terephthalic acid. The photogenerated hydroxyl radicals react with terephthalic acid and form fluorescent 2-hydroxyterephthalic acid.[50,51] 49.8 mg of terephthalic acid was dissolved in 100 mL of 10 mM NaOH aqueous solution, and then 100 mg of photocatalyst material was added to the above solution. The photocatalyst dispersed solution was irradiated with 400 W metal halide lamp. The emission spectrum (Fig. 9a; excited with 325 nm laser) of the irradiated solution was measured at fixed time intervals. The emission peak at 424 nm seen in Fig. 9a corresponds to the production of 2-hydroxyterephthalic acid under metal halide lamp illumination with TiO_2. The intensity of the peak increased with increase in irradiation time, which confirms the reaction mechanism is through the formed hydroxyl radicals in case of TiO_2. However, in the case of composites, the absence of emission peak (Fig. 9a) at 424 nm, confirms that no hydroxyl radicals are formed.

Because the PbO valence band edge positions are not favorable for formation of hydroxyl radical species, the higher photocatalytic activity of TiO_2/PbO can be attributed to direct oxidation of orange G by photogenerated holes, as shown in Fig. 8. However, in the case of TiO_2, degradation of orange G was found to occur through the oxidation of the photogenerated hydroxyl intermediates. It is reported that the quantum yield of hydroxyl radicals are several orders lesser than photogenerated holes.[52,53] This indicates that the photodegradation of dyes *via*

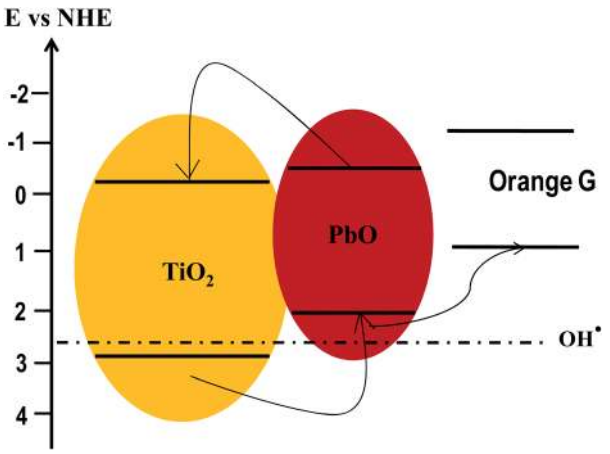

Fig. 8 Schematic illustration of the proposed mechanism to explain the origin of enhanced photocatalytic activity for quantum dot PbO dispersed TiO_2.

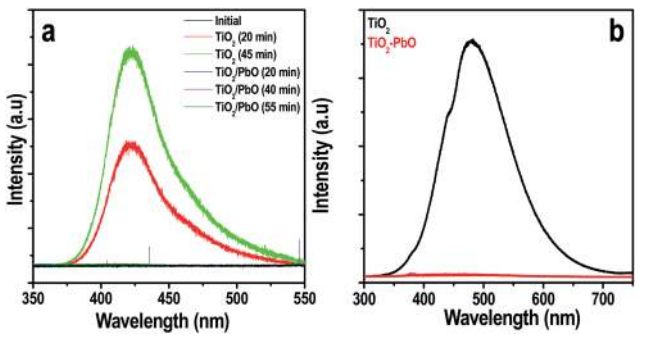

Fig. 9 (a) Photoluminescence spectra measured at various time intervals for the supernatant liquid of the irradiated photocatalyst containing terephthalic acid and (b) cathodoluminescence spectra of synthesized materials, indicating the luminescence quenching in the composite heterostructure.

direct transfer of photogenerated holes is likely to be higher than radical intermediates. This result supports that the engineered band structure provides a way to increase the photoactivity by direct photooxidation of generated holes.

On the basis of above results, the mechanism for photocatalytic activity are proposed (as shown in Fig. 8). The charge migration is favorable for isolation of photogenerated charge carriers in composites.

Many reports have shown that mixed oxides of TiO_2 with suitable band edge positions exhibited higher activity than TiO_2.[18,54,55] However, the enhanced activity is due to separation of generated charge carriers and then followed by production of hydroxyl radicals. In this report, the enhanced photocatalytic activity of PbO/TiO_2 is attributed to direct hole oxidation. The advantage of this heterostructure is the direct dominance of oxidation reactions with photogenerated charge carriers.

To prove the above hypothesis cathodoluminescence CL for the synthesized materials was carried out to determine the emission that indicates the recombination of generated charge carriers. It is observed that in TiO_2, CL is dominated by strong broad visible light emission (Fig. 9b). The CL emission spectrum resembles the photoluminescence spectra of TiO_2, as reported in literature.[56]

The difference in the band gap energy (3.1 eV) calculated form DRS and emission energy form CL is due to Stokes shift because of Frank–Condon effect.[57] The separation of electron–hole pairs are enhanced in the case of the composite material. This causes quenching in the emission (as shown in Fig. 9b), which are responsible for higher photocatalytic activity. These results are in good agreement with band alignment in the formed PbO/TiO_2 heterostructure, as discussed above.

Conclusion

We have synthesized functional composite materials of quantum dot dispersed TiO_2 by a facile sol–gel combustion method. The microscopic studies revealed that the formed quantum dots have intimate contact with TiO_2. The composite exhibits higher photocatalytic activity than TiO_2 under light due to heterostructure energy band alignment. Thus an engineered band structure provides a way to increase the photoactivity by direct photooxidation reaction of generated holes. Therefore, this kind of heterojunction could be a promising approach for further synthesizing new materials that can be used in energy and environmental applications.

Acknowledgements

NR thanks DST, Government of India for financial support. The T20 is a part of the Advanced Facility for Microscopy and Microanalysis at IISc. The FESEM equipped with Mono CL, XPS and the solar simulator are a part of the MNCF, CeNSE at IISc.

References

1 A. Fujishima and K. Honda, *Nature*, 1972, **238**, 37–38.
2 A. L. Linsebigler, G. Lu and J. T. Yates Jr, *Chem. Rev.*, 1995, **95**, 735–758.
3 M. R. Hoffmann, S. T. Martin, W. Choi and D. W. Bahnemann, *Chem. Rev.*, 1995, **95**, 69–96.
4 Y. Aykut, C. Saquing, B. Pourdeyhimi, G. N. Parsons and S. A. Khan, *ACS Appl. Mater. Interfaces*, 2012, **4**, 3837–3845.
5 X. Chen, L. Liu, P. Y. Yu and S. S. Mao, *Science*, 2011, **331**, 746–750.
6 J. S. Lee, K. H. You and C. B. Park, *Adv. Mater.*, 2012, **24**, 1084–1088.
7 S. Sontakke, C. Mohan, J. Modak and G. Madras, *Chem. Eng. J.*, 2012, **189**, 101–107.
8 F. Zuo, K. Bozhilov, R. J. Dillon, L. Wang, P. Smith, X. Zhao, C. Bardeen and P. Feng, *Angew. Chem., Int. Ed.*, 2012, **124**, 6327–6330.
9 J. Yu, Y. Su and B. Cheng, *Adv. Funct. Mater.*, 2007, **17**, 1984–1990.
10 G. Tian, H. Fu, L. Jing and C. Tian, *J. Hazard. Mater.*, 2009, **161**, 1122–1130.
11 T. Tachikawa, S. Yamashita and T. Majima, *J. Am. Chem. Soc.*, 2011, **133**, 7197–7204.
12 J. Pan, G. Liu, G. Q. M. Lu and H. M. Cheng, *Angew. Chem., Int. Ed.*, 2011, **50**, 2133–2137.
13 Z. Xiong and X. S. Zhao, *J. Am. Chem. Soc.*, 2012, **134**, 5754–5757.
14 J. Papp, S. Soled, K. Dwight and A. Wold, *Chem. Mater.*, 1994, **6**, 496–500.
15 M. E. Simonsen, Z. Li and E. G. Søgaard, *Appl. Surf. Sci.*, 2009, **255**, 8054–8062.
16 S. K. Choi, S. Kim, S. K. Lim and H. Park, *J. Phys. Chem. C*, 2010, **114**, 16475–16480.
17 M. Kong, Y. Li, X. Chen, T. Tian, P. Fang, F. Zheng and X. Zhao, *J. Am. Chem. Soc.*, 2011, **133**, 16414–16417.
18 K. Vinodgopal and P. V. Kamat, *Environ. Sci. Technol.*, 1995, **29**, 841–845.
19 T. Ohno, K. Sarukawa and M. Matsumura, *J. Phys. Chem. B*, 2001, **105**, 2417–2420.
20 J. H. Pan and W. I. Lee, *Chem. Mater.*, 2006, **18**, 847–853.
21 B. Naik, S. Martha and K. M. Parida, *Int. J. Hydrogen Energy*, 2011, **36**, 2794–2802.
22 J. Zhang, J. H. Bang, C. Tang and P. V. Kamat, *ACS Nano*, 2009, **4**, 387–395.
23 L. Etgar, D. Yanover, R. K. Čapek, R. Vaxenburg, Z. Xue, B. Liu, M. K. Nazeeruddin, E. Lifshitz and M. Grätzel, *Adv. Funct. Mater.*, 2012, **23**, 2736–2741.
24 X. Chen and S. S. Mao, *Chem. Rev.*, 2007, **107**, 2891–2959.
25 Z. Zhang, C.-C. Wang, R. Zakaria and J. Y. Ying, *J. Phys. Chem. B*, 1998, **102**, 10871–10878.
26 W. Zhou, L. Gai, P. Hu, J. Cui, X. Liu, D. Wang, G. Li, H. Jiang, D. Liu and H. Liu, *CrystEngComm*, 2011, **13**, 6643–6649.
27 D. C. Hurum, A. G. Agrios, K. A. Gray, T. Rajh and M. C. Thurnauer, *J. Phys. Chem. B*, 2003, **107**, 4545–4549.
28 D. Yang, H. Liu, Z. Zheng, Y. Yuan, J. Zhao, E. R. Waclawik, X. Ke and H. Zhu, *J. Am. Chem. Soc.*, 2009, **131**, 17885–17893.
29 P. H. Mutin and A. Vioux, *Chem. Mater.*, 2009, **21**, 582–596.
30 B. Mukherjee, C. Karthik and N. Ravishankar, *J. Phys. Chem. C*, 2009, **113**, 18204–18211.

31 K. Nagaveni, M. Hegde, N. Ravishankar, G. Subbanna and G. Madras, *Langmuir*, 2004, **20**, 2900–2907.
32 S. Polisetti, P. A. Deshpande and G. Madras, *Ind. Eng. Chem. Res.*, 2011, **50**, 12915–12924.
33 Z. A. Munir and U. Anselmi-Tamburini, *Mater. Sci. Rep.*, 1989, **3**, 277–365.
34 Z. Zhang, X. Zhong, S. Liu, D. Li and M. Han, *Angew. Chem., Int. Ed.*, 2005, **117**, 3532–3536.
35 M. Salavati-Niasari, F. Mohandes and F. Davar, *Polyhedron*, 2009, **28**, 2263–2267.
36 A. S. Barnard and P. Zapol, *J. Phys. Chem. B*, 2004, **108**, 18435–18440.
37 J. Joo, S. G. Kwon, T. Yu, M. Cho, J. Lee, J. Yoon and T. Hyeon, *J. Phys. Chem. B*, 2005, **109**, 15297–15302.
38 Y. Jun, M. F. Casula, J. H. Sim, S. Y. Kim, J. Cheon and A. P. Alivisatos, *J. Am. Chem. Soc.*, 2003, **125**, 15981–15985.
39 C. T. Dinh, T. D. Nguyen, F. Kleitz and T. O. Do, *ACS Nano*, 2009, **3**, 3737.
40 M. Staszewski, Z. Myczkowski, K. Bilewska, R. Sosinski, M. Lis, M. Czepelak and D. Kolacz, *Journal of Achievements in Materials and Manufacturing Engineering*, 2012, **52/1**, 39–46.
41 N. C. Jeong, C. Prasittichai and J. T. Hupp, *Langmuir*, 2011, **27**, 14609–14614.
42 Y. Luo, J. Luo, J. Jiang, W. Zhou, H. Yang, X. Qi, H. Zhang, H. J. Fan, D. Y. W. Yu, C. M. Li and T. Yu, *Energy Environ. Sci.*, 2012, **5**, 6559–6566.
43 H. Wang, A. Zhou, F. Peng, H. Yu and J. Yang, *J. Colloid Interface Sci.*, 2007, **316**, 277–283.
44 M. Thommes, *Chem. Ing. Tech.*, 2010, **82**, 1059–1073.
45 J. B. Joo, Q. Zhang, M. Dahl, I. Lee, J. Goebl, F. Zaera and Y. Yin, *Energy Environ. Sci.*, 2012, **5**, 6321–6327.
46 S. Chen and L.-W. Wang, *Chem. Mater.*, 2012, **24**, 3659–3666.
47 M. Long, W. Cai, J. Cai, B. Zhou, X. Chai and Y. Wu, *J. Phys. Chem. B*, 2006, **110**, 20211–20216.
48 Y. Xu and M. A. A. Schoonen, *Am. Mineral.*, 2000, **85**, 543–556.
49 S. Nam and P. G. Tratnyek, *Water Res.*, 2000, **34**, 1837–1845.
50 T. Hirakawa and Y. Nosaka, *Langmuir*, 2002, **18**, 3247–3254.
51 G. Liu, C. Sun, H. G. Yang, S. C. Smith, L. Wang, G. Q. M. Lu and H.-M. Cheng, *Chem. Commun.*, 2010, **46**, 755–757.
52 M. Y. Guo, A. M. C. Ng, F. Liu, A. B. Djurišić, W. K. Chan, H. Su and K. S. Wong, *J. Phys. Chem. C*, 2011, **115**, 11095–11101.
53 K.-i. Ishibashi, A. Fujishima, T. Watanabe and K. Hashimoto, *J. Photochem. Photobiol., A*, 2000, **134**, 139–142.
54 F. Riboni, L. G. Bettini, D. W. Bahnemann and E. Selli, *Catal. Today*, 2013, **209**, 28–34.
55 K. Vinodgopal, I. Bedja and P. V. Kamat, *Chem. Mater.*, 1996, **8**, 2180–2187.
56 R. Vinu and G. Madras, *Appl. Catal., A*, 2009, **366**, 130–140.
57 M. Rahman, K. Krishna, T. Soga, T. Jimbo and M. Umeno, *J. Phys. Chem. Solids*, 1999, **60**, 201–210.